*Allegato II*

# RELAZIONE ANNUALE DI SINTESI

**RELAZIONE ANNUALE DI SINTESI**

*(La presente Relazione deve essere compilata e firmata dal Dottorando)*

**ATTIVITA' DI RICERCA RELATIVA ALLA II ANNUALITA'**

| | |
|---|---|
| **DOTTORANDO** | DOWLATABADI MITRA |
| **CUP** | J92B23001590007 |
| **CORSO DI DOTTORATO** | FISICA |
| **ANNO ACCADEMICO** | 2024-2025 |
| **COORDINATORE CORSO** | LONGO FRANCESCO |
| **CODICE BORSA** | 39-034-33-DOT1333595-10438 |

Il sottoscritto, in piena coerenza con le tematiche previste dal progetto nell'ambito del quale è stata finanziata la borsa di dottorato e nel rispetto dell'impegno assunto ad effettuare i periodi di attività previsti dal percorso di dottorato finanziato a valere del PNRR, consapevole della responsabilità penale cui può andare incontro in caso di dichiarazione falsa o comunque non corrispondente al vero (art. 76 del D.P.R. n. 445 del 28/12/2000), ai sensi del D.P.R. n. 445 del 28/12/2000 e ss.mm.ii.

**ATTESTA**

1. che le principali attività svolte nella II annualità sono di seguito riassunte:

| **ATTIVITÀ SVOLTE** |
|---|
| Topological superconductors (TSCs) have attracted considerable interest due to their potential to host Majorana excitations and enabling fault-tolerant quantum computation. Since intrinsic TSCs are extremely rare, an effective strategy is to engineer them artificially by combining conventional superconductors with materials such as topological insulators, where superconductivity can be induced via the proximity effect [1–4].<br><br>The goal of this work is to design artificial TSCs from first principles. To achieve this, we employ advanced computer approaches that combine density functional theory (DFT), many-body perturbation theory (MBPT), and Wannier-based Bogoliubov–de Gennes (BdG) methods. This framework enables a direct connection between the microscopic electronic structure and superconducting properties in realistic heterostructures.<br><br>During the second year of my PhD, I completed two research visits: six months at EPFL with the THEOS group under the supervision of Prof. Nicola Marzari, and two months at CNR-NANO in Modena under the supervision of Dr. Andrea Ferretti. These collaborations broadened my expertise in Wannier functions and embedding techniques. In addition, I participated in the "YAMBO School", where I received hands-on training in calculating spectral and quasiparticle properties, which are essential for analyzing many-body interactions and spin-orbit coupling in |

complex heterostructures. I also attended the "PSI-K Conference" in Lausanne and received a commendation for my poster presentation (Poster commendations).

Building on the expertise developed during these research visits, we focused on the first-principles modelling of a Nb/$Bi_2Te_3$ heterostructure. After successfully Wannierizing both Nb and $Bi_2Te_3$ , we constructed a slab geometry consisting of four Nb(111) layers and three quintuple layers (QLs) of $Bi_2Te_3$ , as shown in Fig. 1(a). The total energy was optimized with respect to the interlayer distance between the two materials while keeping the vacuum thickness fixed. In all calculations, atomic positions were fully relaxed except for the topmost and bottom layers, which were constrained to simulate bulk termination.

For the Wannierization, a total of 234 Wannier functions were constructed using an 8 ×8 ×1 k-point grid of the Brillouin zone. The Wannier basis included NB p- and d-orbitals, as well as p-orbitals for Bi and Te, explicitly incorporating spin–orbit coupling. As shown in Fig. 1(b), the Wannier-interpolated bands reproduce the DFT results accurately near the Fermi level.

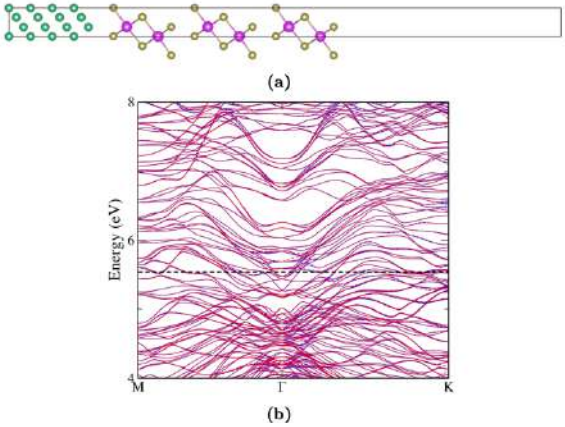


***Figure 1*** *(a) Crystal structure of the Nb(111)/ $Bi_2Te_3$ heterostructure. (b) Calculated electronic band structure. The dashed black line indicates the Fermi level, the solid blue lines correspond to the DFT bands, and the dashed red lines represent the Wannier-interploated bands*

Understanding proximity-induced superconductivity requires a unified description of both normal-state and superconducting properties. In particular, an accurate treatment of the electronic band structure, density of states, and both normal and anomalous charge densities is essential for capturing the spatially inhomogeneous nature of the proximity effect in realistic heterostructures.

A major challenge in this project arises from the large number of atoms in the heterostructure and the presence of strong spin–orbit coupling, which render fully first-principles Migdal-Eliashberg (ME) calculations computationally prohibitive. To overcome this limitation, we combined DFT with the BdG formalism, implemented in our Python code BdGWPy. The BdG approach is a Hartree–Fock-like mean-field theory that generalizes BCS theory to inhomogeneous superconducting systems [5].
For singlet pairing symmetry, the effective mean-field Hamiltonian is

$$H_{\text{eff}} = \sum_{i,j,\sigma,\sigma'} c^{\dagger}_{i\sigma} h_{i\sigma,j\sigma'} c_{j\sigma'} + \sum_{i,j} \left[ \Delta_{ij} c^{\dagger}_{i\uparrow} c^{\dagger}_{j\downarrow} + \Delta^{*}_{ij} c_{i\uparrow} c_{j\downarrow} \right] + E_{\text{const}}, \qquad (1)$$

where $h_{i\sigma,j\sigma'}$ is the effective single-particle Hamiltonian and $\Delta_{ij}$ the singlet pairing potential which satisfies the self-consistency condition

$$\Delta_{ij} = U\chi_{ij} \tag{2}$$

with U the effective interaction strength and $\chi_{ij}$the anomalous density. The latter is defined as

$$\chi_{ij} = \sum_{n}{}' \left(u^n_{i\uparrow} v^{n*}_{j\downarrow} f(-E_n) - u^n_{j\downarrow} v^{n*}_{i\uparrow} f(E_n)\right), \tag{3}$$

where $u^n_{i\sigma}$ and $v^n_{i\sigma}$ are the quasiparticle wavefunctions, $E_n$ are the corresponding quasiparticle energies, and $f(E_{n)}$ is the Fermi-Dirac distribution at temperature $T$:

$$f(E_n) = \frac{1}{\exp(E_n/k_B T) + 1} \tag{4}$$

Finally, the pairing potential is restricted to states lying within the Debye energy window:

$$\Delta = \begin{cases} \Delta, & -\hbar\omega_D \le E_n \le \hbar\omega_D \\ 0, & \text{otherwise} \end{cases} \tag{5}$$

To determine the effective interaction strength U, we first extracted the effective pairing potential of bulk Nb at $T \approx 0\ K$ from ME calculations performed using EPW. This pairing potential, together with the Wannier Hamiltonian of Nb, was used as the initial input for constructing the BdG Hamiltonian. By iteratively evaluating the anomalous density according to Eq. (3) and inserting into the self-consistency condition of Eq. (2), we obtained a consistent estimate of U. This value was subsequently employed to study the temperature dependence of the pairing potential within the BdG framework. The same procedure also provides an estimate of the superconducting critical temperature $T_c$, defined as the temperature at which the pairing potential vanishes. The overall computational workflow is summarized in Fig. 2.

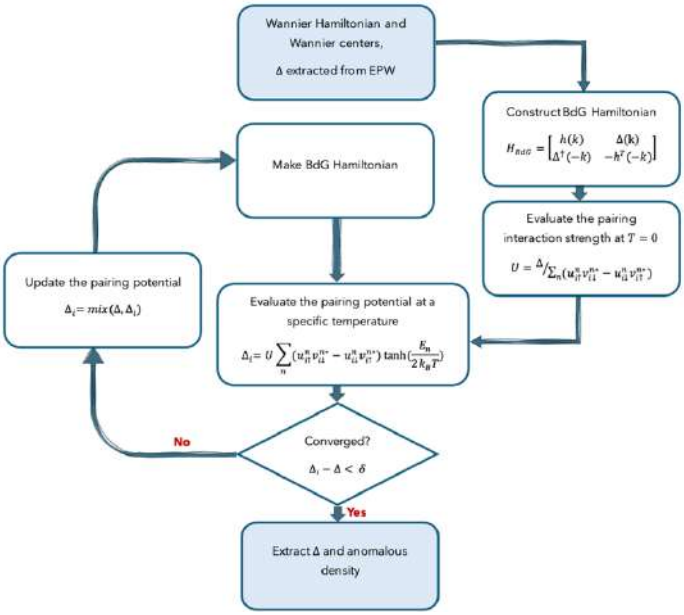


***Figure 2*** *Iterative workflow: starting from first-principles MBPT calculations within the ME framework using EPW, leading to self-consistent solutions of the BdG equations for an s-wave superconductor.*

We first assessed the convergence of the pairing potential with respect to the number of k-points. As shown in Fig. 3(a), convergence is achieved using approximately 216,000 k-points on a uniform grid for the bulk Nb. However, applying such dense sampling to heterostructure with a large number of atoms would be computationally unfeasible. To address this limitation, we implemented a stochastic Monte Carlo sampling scheme, in which k-points are selected according to a probability distribution that decays exponentially with their energy distance from the Fermi level,

$$P(k) \propto exp\left[-\frac{min|\varepsilon_n(k)-\mu|}{\sigma}\right] \quad (6)$$

Where $\sigma$ is a tunable energy scale. Using this approach, we were able to reproduce the dense-grid results with good accuracy using only 7447 k-points.

In Fig. 3(b), we compare the pairing potential obtained within the BdG framework with results from ME theory calculated using EPW. To facilitate a direct comparison and benchmark our approach against conventional theory, both datasets were fitted using the standard BCS expression for the temperature dependence of the pairing potential,

$$\Delta(T) = \Delta(0)\tanh\left(1.74\sqrt{\frac{T_c}{T}-1}\right). \quad (7)$$

The good agreement between the BdG and ME results demonstrates that the Wannier-based BdG framework accurately captures the superconducting properties of the bulk Nb while remaining computationally efficient.

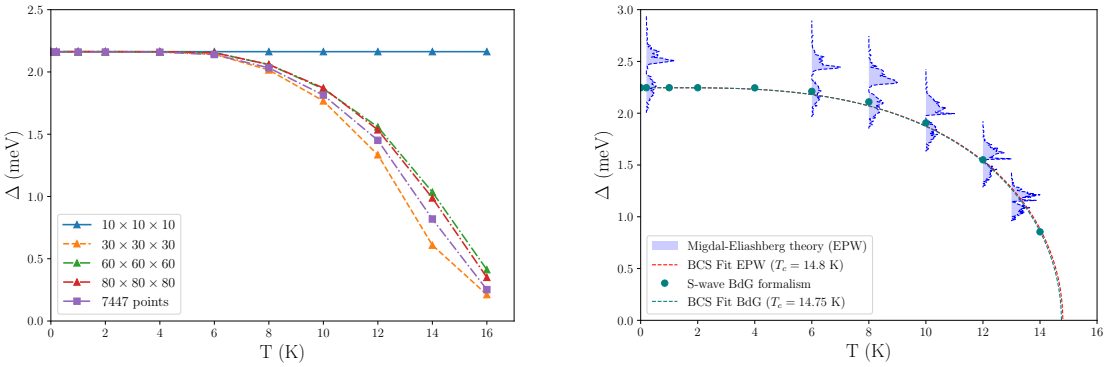


***Figure 3*** *(a) Convergence of the pairing potential of bulk Nb with respect to the number of k-points. (b) Temperature dependence of the pairing potential from EPW (ME theory) compared with the BdG framework.*

Having validated the Wannier-based BdG framework for the bulk Nb, we next applied it to the $Nb/Bi_2Te_3$ heterostructure. In this case, the effective interaction strength U was fixed to

$$U = \begin{cases} U_{Nb-bulk}, & \text{on the Nb side} \\ 0, & \text{on the } Bi_2Te_3 \text{ side} \end{cases} \quad (8)$$

reflecting the fact that superconductivity originates exclusively from the Nb layers, while $Bi_2Te_3$ acts as a normal material in which superconducting correlations are induced via the proximity effect.

Using the interaction strength defined in Eq. (8), we computed the singlet anomalous density as defined in Eq. (3) at low temperature $T \approx 0\ K$. Fig. 4 shows the layer-averaged anomalous density across the $Nb/Bi_2Te_3$ heterostructure. As expected, superconducting correlations are strongest within the Nb layers and decay progressively into the $Bi_2Te_3$ region. The characteristic decay length increases with the number of QLs, reflecting the penetration of proximity-induced superconductivity into the topological insulator.

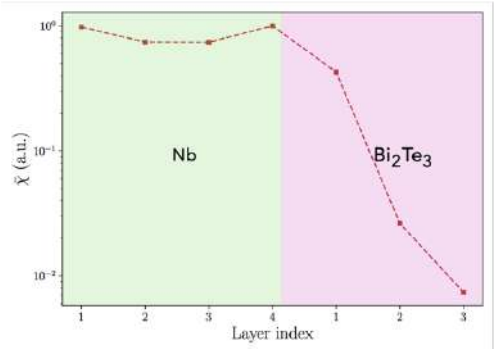


***Figure 4*** *Layer-averaged anomalous density in the $Nb/Bi_2Te_3$ heterostructure at $T \approx 0\ K$. The dacay of superconducting correlations into the topological insulator regioni s evident.*

So far, the superconducting properties of the $Nb/Bi_2Te_3$ heterostructure have been investigated using a momentum-independent (constant) pairing interaction. While this approximation is sufficient to capture the essential features of proximity-induced superconductivity, a more complete and realistic description requires accounting for the momentum dependence of the pairing interaction. For this reason, we have extended the BdG formalism to include a k-dependent pairing potential, in which the effective interaction is described by a non-local kernel rather than a single constant $U$.

Within this generalized framework, the pairing potential at a given momentum is obtained from a convolution of the interaction kernel with the anomalous density in momentum space,

$$\hat{\Delta}_{ij}(k) = \frac{1}{N}\sum_{k'} U(k-k')\hat{\chi}_{ij}(k') \qquad (9)$$

This formulation allows us to capture anisotropy and non-local effects in the superconducting pairing, which are expected to play an important role in complex heterostructures. The implementation of this momentum-dependent formalism is currently in progress.

Alongside the superconducting proximity-effect studies, we also investigated the microscopic role of the heterostructure interface. The chemical and electronic structure at the interface between the superconductor and the topological insulator plays a crucial role in determining the magnitude and character of the proximity-induced superconducting gap [6]. In particular, the electrostatic potential profile across the interface governs the relative alignment of electronic states in the two materials. Such band alignment is a key factor for stabilizing topological excitations, including Majorana zero modes. A convenient and physically transparent quantity for characterizing this alignment is the work function, which measures the energy required to remove an electron from the Fermi level into the vacuum.

The work function is obtained from the electrostatic potential, which includes contributions from both the electronic Hartree potential and the ionic Coulomb potential [7]. Two standard approaches were employed in this work:

- In the first approach, referred to as the direct slab method, the work function is defined as the difference between the vacuum potential level and the Fermi energy of the slab,

$$\Phi = V_{\text{vac}}^{\text{slab}} - E_F^{\text{slab}}. \tag{10}$$

- In the second approach, known as the bulk reference method, the slab Fermi energy is referenced to the average electrostatic potential of the bulk material:

$$\Phi = V_{\text{vac}}^{\text{slab}} - \left(V_{\text{metal}}^{\text{slab}} + E_F^{\text{bulk}} - V^{\text{bulk}}\right), \tag{11}$$

where $V_{metal}^{slab}$ is the macroscopic average of the electrostatic potential at the slab center.

We first applied the two work-function evaluation methods to Nb(111) slabs with varying thickness. The calculated values are summarized in Table I. In this case, the bulk reference method shows better agreement with experimental data, which range from 4.08 to 4.66 eV [8, 9], compared to the direct slab method.

We next considered $Bi_2Te_3$ slab, with the calculated work function values reported in Table II. In this case, the direct slab method reproduces the experimental work-function values (5.28–5.31 eV [10]) reasonably well, whereas the bulk reference method yields less accurate results. This discrepancy originates from the intrinsic limitations of DFT in describing the spectral properties and band gaps of semiconductors. In particular, the position of the bulk electrostatic potential relative to the band edges is not accurately captured within standard DFT. Overcoming this limitation requires going beyond DFT, for example by employing many-body approaches such as GW corrections.

| Number of Layers | $\Phi^{\text{slab}}$ (eV) | $\Phi^{\text{bulk-ref}}$ (eV) |
|---|---|---|
| 4 | 3.68 | 4.14 |
| 6 | 3.71 | 4.17 |
| 8 | 3.69 | 4.16 |
| 10 | 3.69 | 4.12 |
| 12 | 3.70 | 4.13 |
| 25 | 3.69 | 4.14 |

***Table I*** *Calculated work function of Nb(111) slabs. $\phi^{slab}$ is obtained using the direct slab method, while $\phi^{bulk-ref}$ is obtained using the bulk refrence method.*

| Number of QLs | $\Phi^{\text{slab}}$ (eV) | $\Phi^{\text{bulk-ref}}$ (eV) |
|---|---|---|
| 3 | 5.17 | 4.30 |
| 5 | 5.10 | 4.30 |
| 7 | 5.07 | 4.30 |
| 10 | 5.06 | 4.30 |

***Table II*** *Calculated work function of $Bi_2Te_3$ slabs using both direct slab and bulk refrence methods.*

The significant mismatch between the work function of Nb and $Bi_2Te_3$ implies a transfer of charge across the interface, from Nb (lower $\phi$) to $Bi_2Te_3$ (higher $\phi$). This transfer leads to band bending near the interface and modifies the local electronic structure of the heterostructure. Such interface-induced electrostatic effects are expected to influence the strength and spatial extent of proximity-induced superconductivity, as well as the emergence of topological interface states.

The layer-resolved local density of states (LDOS), shown in Fig. 5, confirms this interpretation. A downward shift of the electronic bands is observed at the $Bi_2Te_3$ surface, consistent with electron transfer from the Nb substrate into the topological insulator. This behavior reflects the band bending induced by the work-function mismatch and is in agreement with previous theoretical studies [9]. Importantly, topological surface states are clearly visible at the Nb/Bi2Te3 interface, whereas no surface state is observed on the opposite side of the $Bi_2Te_3$ slab for a thickness of three QLs, indicating that the interface electronic structure is strongly influenced by proximity to the superconductor.

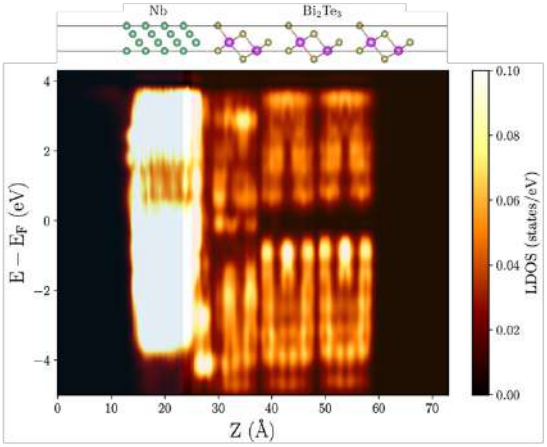


***Figure 5*** *The LDOS of the Nb/$Bi_2Te_3$ heterostructure, showing downward band bending at the topological insulator surface due to charge transfer from Nb.*

**References:**

[1] L. Fu and C. L. Kane, Physical Review Letters, vol. 100, no. 9, p. 096407, 2008.
[2] P. Zareapour, A. Hayat, S. Y. F. Zhao, et al., Nature Communications, vol. 3, no. 1, p. 1056, 2012.
[3] M.-X. Wang, C. Liu, J.-P. Xu, F. Yang, et al., Science, vol. 336, no. 6077, pp. 52–55, 2012.
[4] D. Fl¨ototto, Y. Ota, Y. Bai, C. Zhang, et al., Science Advances, vol. 4, no. 4, p. eaar7214, 2018.
[5] J.-X. Zhu, Bogoliubov–de Gennes method and its applications, vol. 924. Springer, 2016.
[6] P. R¨außmann and S. Bl¨ugel, arXiv preprint arXiv:2208.14289, 2022.
[7] C. J. Fall, N. Binggeli, and A. Baldereschi, Journal of Physics: Condensed Matter, vol. 11, p. 2689, apr 1999.
[8] G. N. Derry, M. E. Kern, and E. H. Worth, Journal of Vacuum Science & Technology A, vol. 33, no. 6, 2015.
[9] K. Nagaoka, H. Ogawa, N. Arai, et al., Surface Science, vol. 357-358, pp. 218–221, 1996.
[10] D. Haneman, Journal of Physics and Chemistry of Solids, vol. 11, no. 3-4, pp. 205–214, 1959.

| PERIODO SOSPENSIONE ATTIVITA’ | |
|---|---|
| DAL | AL |

2. che le sopra descritte attività:

a. non arrecano danno significativo a nessuno dei sei obiettivi ambientali indicati all'art. 17 del Reg. (UE) 2020/852, e di seguito richiamati:
   i. Mitigazione dei cambiamenti climatici,
   ii. Adattamento ai cambiamenti climatici;
   iii. Uso sostenibile e protezione delle risorse idriche e marine;
   iv. Transizione verso l'economia circolare, con riferimento anche a riduzione e riciclo dei rifiuti;
   v. Prevenzione e riduzione dell'inquinamento dell'aria, dell'acqua o del suolo;
   vi. Protezione e ripristino della biodiversità e degli ecosistemi.
b. non ricadono tra le seguenti attività di ricerca cosiddetta *"brown"* in conformità alla Comunicazione della Commissione UE 2021/C 58/01 *"Orientamenti tecnici sull'applicazione del principio DNSH"*;
   i. attività connesse ai combustibili fossili, compreso l'uso a valle;
   ii. attività nell'ambito del sistema di scambio di quote di emissione dell'UE (ETS) che generano emissioni di gas a effetto serra previste non inferiori ai pertinenti parametri di riferimento;
   iii. attività connesse alle discariche di rifiuti agli inceneritori e agli impianti di trattamento meccanico biologico;
   iv. attività nel cui ambito lo smaltimento a lungo termine dei rifiuti potrebbe causare un danno all'ambiente.
c. sono conformi alla pertinente normativa ambientale dell'UE e nazionale

Data

07/01/2026

Firma